ILASS-Americas 22nd Annual Conference on Liquid Atomization and Spray Systems, Cincinnati, OH, May 2010

Simulating Electrohydrodynamic Atomization for Fuel Injection

B. Van Poppel[*], O. Desjardins, and J.W. Daily
Department of Mechanical Engineering
University of Colorado, Boulder, CO 80309

Abstract

Electrohydrodynamic flows and sprays hold several potential benefits for combustion systems, such as the production of smaller droplets, a wider spray cone, and the ability to control or "tune" the spray. Nevertheless, key questions regarding the complex interactions among electrostatic charge, electric fields, and the dynamics of atomizing liquids remain unanswered. In this work, a recently developed numerical scheme is used to simulate primary atomization for an electrically charged liquid hydrocarbon fuel. This novel technique is implemented within a conservative finite difference scheme of high-order accuracy that employs state-of-the-art interface transport techniques ideally suited for simulating multiphase flows. The model is applied in direct numerical simulation of a charged liquid kerosene jet and qualitatively compared to experiments. To more accurately replicate the hydrodynamic inflow conditions, different preliminary inlet simulations are conducted and discussed.

---

[*] Corresponding Author: bret.vanpoppel@colorado.edu

Introduction

Electrohydrodynamics, or EHD, may provide a viable means to enhance combustion. EHD may enable improved spray control and finer atomization, thereby offering efficient enhancements that could benefit a broad range of engines and even other, non-combustion applications. One application of immediate interest to the authors is the development of inexpensive fuel injection systems for the small (200 cm^3) internal combustion engine class. EPA reports show that this class of engines emits pollutants at high rates [1]. Compounding the challenge of fuel injecting these engines is their low cost, suggesting that miniaturization of automotive-type fuel injection systems would be far too expensive for market adoption [2].

EHD flows and sprays have drawn considerable interest over the past three decades, progressing from pioneering work by Kim and Turnbull [3]. Shrimpton and co-workers have studied the technique of "charge injection" through experimental [4, 5, 6, 7, 8, 9] and numerical [10, 11] investigations. Notwithstanding these efforts, the complex interactions among electrostatic charge, electric fields, and the dynamics of atomizing liquids are not well understood. Considering the challenges and expense of experiments, high-fidelity numerical simulations should be able to provide some clarity to the underlying fundamentals and dynamics of EHD atomization. To this end, Van Poppel, Desjardins, and Daily [12, 13] recently developed a novel methodology for simulating multiphase EHD in liquid dielectric hydrocarbon fuels. The scheme leverages the ghost fluid method (GFM) to accurately solve the electric potential Poisson equation and also uses the GFM to provide a numerically sharp representation for the EHD interface conditions. The methodology is robust and capable of handling large density ratios. The numerical scheme captures the singular nature of the surface tension force, and accurately transports the phase interface using state-of-the-art interface tracking techniques.

The present work employs the recently developed computational scheme to perform fully three-dimensional direct numerical simulations of electrically charged liquid jets and qualitatively compare simulation results with experiments performed by Shrimpton and co-workers [6, 7, 8]. Multiphase simulations are performed using different inflows, including a bulk inflow, a fully turbulent inflow using the results of a turbulent pipe preliminary simulation, and a realistic charge injection nozzle modeled after nozzles employed in experiments. Effects of different inflows are compared to experimental results.

Mathematical Formulation

To mitigate the challenge of modeling the full set of governing equations, charge is assumed constant through a time scale analysis. For the inertial flows of interest in this work, the advection time scale is expected to be the governing time scale, which is much shorter than the space charge relaxation time scale for the highly insulating fuels considered here. We assume constant volumetric charge, using a time scale analysis detailed in [12], and employ this assumption to simplify some of the governing equations and interfacial boundary conditions.

Conservation of mass and momentum for a variable density, low Mach number flow are given as

$$\begin{aligned} \frac{\partial \rho}{\partial t} + \nabla \cdot (\rho \boldsymbol{u}) &= 0, & (1) \\ \frac{\partial \rho \boldsymbol{u}}{\partial t} + \nabla \cdot (\rho \boldsymbol{u} \otimes \boldsymbol{u}) &= -\nabla p \\ &+ \nabla \cdot (\boldsymbol{\sigma}^f + \boldsymbol{\sigma}^e) + \rho \boldsymbol{g}, & (2) \end{aligned}$$

where $\boldsymbol{u}$ is the velocity field, p is the hydrodynamic pressure, ρ is the mass density, and $\boldsymbol{g}$ is gravitational acceleration. The viscous stress tensor, $\boldsymbol{\sigma}^f$, is given by

$$\boldsymbol{\sigma}^f = \mu \left(\nabla \boldsymbol{u} + \nabla \boldsymbol{u}^t \right) - \frac{2}{3} \mu \nabla \cdot \boldsymbol{u} \mathbb{I}, \qquad (3)$$

with $\mathbb{I}$ the identity tensor and μ is the dynamic viscosity. The electric body force, $\boldsymbol{f}_e$, is given as,

$$\boldsymbol{f}_e = q\boldsymbol{E} - \frac{1}{2} \boldsymbol{E}^{\boldsymbol{2}} \nabla \epsilon + \nabla \left(\frac{1}{2} \rho \frac{\partial \epsilon}{\partial \rho} \boldsymbol{E}^2 \right), \qquad (4)$$

where ϵ is the electric permittivity, q is a volumetric electric charge density, and $\boldsymbol{E}$ is the electric field vector. The three terms of $\boldsymbol{f}_e$ represent the Coulomb force, the dielectric force, and the electrostrictive force, respectively. Assuming incompressibility and material homogeneity within a phase, $\boldsymbol{f}_e$ reduces to the Coulomb force in the bulk [14, 15] as

$$\boldsymbol{f}_e = q\boldsymbol{E}. \qquad (5)$$

The electric displacement vector, $\boldsymbol{D}$, is assumed to vary linearly with the electric field vector, as

$$\boldsymbol{D} = \epsilon \boldsymbol{E}. \qquad (6)$$

The electric field vector is irrotational, hence it can be expressed as the gradient of the scalar electric potential, ϕ, as

$$\boldsymbol{E} = -\nabla \phi. \qquad (7)$$

The Gauss law can be employed for a dielectric material to relate the electric displacement vector to the volumetric charge, as

$$\nabla \cdot \boldsymbol{D} \;=\; \nabla \cdot \epsilon \boldsymbol{E} = -\nabla \cdot (\epsilon \nabla \phi) = q. \qquad (8)$$

Charge conservation and current density are described by

$$\frac{\partial q}{\partial t} \;+\; \nabla \cdot \boldsymbol{J} = 0, \qquad (9)$$

$$\boldsymbol{J} \;=\; \mu_i q \boldsymbol{E} - D_i \nabla q + q\boldsymbol{u}, \qquad (10)$$

where $\boldsymbol{J}$ is the current density, D_i is the molecular diffusion coefficient and μ_i is the ionic mobility coefficient. Uniform space charge reduces these equations to solenoidal current density that convects with the flow, as

$$\nabla \cdot \boldsymbol{J} \;=\; 0, \qquad (11)$$

$$\boldsymbol{J} \;=\; q\boldsymbol{u}. \qquad (12)$$

The interface boundary and jump conditions are essential to capturing the dominant mechanisms influencing the flow and atomization. While the velocity and tangential electric field components are continuous across the interface, the mass density, viscosity, and electric displacement vector experience jumps, described by

$$[\boldsymbol{u} \cdot \boldsymbol{n}]_\Gamma \;=\; 0, \qquad (13)$$

$$[\boldsymbol{u} \cdot \boldsymbol{t}_i]_\Gamma \;=\; 0, \quad \text{for } i = 1, 2 \qquad (14)$$

$$[\rho]_\Gamma \;=\; \rho_l - \rho_g, \qquad (15)$$

$$[\mu]_\Gamma \;=\; \mu_l - \mu_g, \qquad (16)$$

$$[\epsilon]_\Gamma \;=\; \epsilon_l - \epsilon_g, \qquad (17)$$

$$[\boldsymbol{D}]_\Gamma \;=\; \boldsymbol{n} \cdot [\epsilon \boldsymbol{E}]_\Gamma = q_s, \qquad (18)$$

$$\boldsymbol{n} \times [\boldsymbol{E}]_\Gamma \;=\; 0, \qquad (19)$$

where $[(\cdot)]_\Gamma$ represents the jump of "$(\cdot)$" across the interface, Γ, and for example, $[\boldsymbol{D}]_\Gamma$ represents the jump of the electric displacement vector across the interface, $\boldsymbol{n}$ and $\boldsymbol{t}$ represent the normal and tangential vector components at the interface, subscripts l and g represent quantities in the liquid and gas phases, respectively, and q_s the surface charge. The assumption of constant volumetric space charge implies negligible surface charge, suggesting that the normal component of the electric displacement vector is continuous. However, the jump in electric permittivity across the phase interface imposes a discontinuity in the normal component of the electric field, and Eq. (18) can be written as

$$\boldsymbol{n} \cdot [\boldsymbol{D}]_\Gamma = \boldsymbol{n} \cdot [\epsilon \boldsymbol{E}]_\Gamma = [\epsilon E_n]_\Gamma = 0. \qquad (20)$$

A direct consequence of the irrotational jump condition, Eq. (19), ensures that the tangential components of the electric field, and therefore the electric potential, ϕ, are continuous,

$$[E_{t_1}]_\Gamma = 0, \quad [E_{t_2}]_\Gamma = 0, \text{ and} \qquad (21)$$

$$[\phi]_\Gamma = 0. \qquad (22)$$

The pressure interface jump condition includes contributions from viscous, electric and surface tension forces, and is represented as

$$-[p]_\Gamma + [\boldsymbol{n}^\mathsf{T} \cdot (\boldsymbol{\sigma}^e + \boldsymbol{\sigma}^f) \cdot \boldsymbol{n}]_\Gamma = -\gamma\kappa, \qquad (23)$$

which can be simplified as

$$[p]_\Gamma - 2[\mu]_\Gamma \boldsymbol{n}^\mathsf{T} \cdot \nabla \boldsymbol{u} \cdot \boldsymbol{n} - \gamma\kappa = \left[\frac{1}{2}\epsilon E_n^2\right]_\Gamma - \left[\frac{1}{2}\epsilon E_{t_i}^2\right]_\Gamma, \qquad (24)$$

where $[p]_\Gamma$ is the jump across the interface, γ the surface tension coefficient, and κ the local interface curvature. The tangential shear stress balance, again employing negligible surface charge, yields

$$\left[\boldsymbol{n}^\mathsf{T} \cdot (\boldsymbol{\sigma}^f) \cdot \boldsymbol{t}_i\right]_\Gamma = 0. \qquad (25)$$

Additional details are provided in [12].

Numerical Approach

All simulations performed in this work employ an in-house code named NGA [16], for which the numerical methods described herein have been implemented in parallel using Message Passing Interface (MPI). NGA extends the family of high order fully conservative finite difference schemes proposed by Morinishi and Vasilyev [17, 18, 19] to variable density low-Mach number flows [16, 20]. These schemes, tailored for DNS and LES, provide excellent accuracy, while retaining exceptional numerical robustness since they discretely conserve mass, momentum, and kinetic energy. A three-dimensional formulation of the black-box multigrid (BBMG) solver [21] is employed to efficiently solve the pressure and electric potential Poisson equations.

To fully capture liquid breakup, the NGA code employs two state-of-the-art interface transport techniques [22, 23], one of which is called Accurate Conservative Level Set, ACLS [22]. This novel methodology combines an improved version of the conservative level set technique introduced in Olsson *et al.* [24] with a ghost fluid approach [25]. By employing a hyperbolic tangent level set function that is transported and re-initialized using fully conservative numerical schemes, mass conservation issues that are known to affect level set methods are greatly reduced. In order to improve the accuracy of the conservative level set method, high order numerical schemes are employed. ACLS is used for all multiphase simulations described in this paper.

Ghost Fluid Method for Electric Potential

The ghost fluid method (GFM) [25] provides a very attractive way of handling discontinuities by using generalized Taylor series expansions that directly include these discontinuities. Because GFM explicitly deals with the density jump, the resulting discretization is not affected by the density ratio. Similarly, the surface tension force can be included directly in the form of a pressure jump, providing an adequate sharp numerical treatment of this singular term. The EHD module solves the electric potential, ϕ, which is an additional variable coefficient Poisson equation given in Eq. (8). In previous work, a generalized Taylor series expansion was employed to provide a sharp implementation for the pressure Laplacian across an interface jump [16, 22, 20]. Using a similar approach, a sharp formulation is employed for the gradient and Laplacian of the electric potential, in either the gas or the liquid phase, to provide an accurate and efficient solution for the electric potential.

EHD Interface Methodology

Even with perfect dielectrics, EHD effects can be noticed due to the strong coupling through the jump conditions at the interface. The right hand side of Eq. (24) shows how the electric stresses contribute to the pressure jump across the interface through the normal and tangential components of the electric field. The NGA code employs a staggered grid methodology, which poses challenges for the solution of the electric potential Poisson equation as well as the EHD jump conditions. The normal vectors are known at the cell centers and the Cartesian components of the electric field are known at the cell faces. Therefore, it is necessary to interpolate the components of the electric field to the cell center, re-construct a cell-centered electric field vector, and subsequently partition this interpolated vector into its normal and tangential components. The GFM is integrated with this scheme to handle interpolation across the inteface. This tri-linear GFM interpolation scheme yields an accurate and efficient numerical solution for the EHD jump conditions.

Implementation of Coulomb Force

The Coulomb force, Eq. (5), is implemented as a face-centered source term in the Navier-Stokes equations. For each Cartesian dimension, charge is computed at each cell face using a height function of the liquid volume fraction according to Eq. (26), and then multiplied by the local face value of the electric field. The height function, $\lambda_{i,j,k+\frac{1}{2}}$, is defined as

$$\lambda_{i,j,k+\frac{1}{2}} = \begin{cases} 1 & \text{if } G_{i,j,k} \text{ and } G_{i+1,j,k} \geq 0, \\ 0 & \text{if } G_{i,j,k} \text{ and } G_{i+1,j,k} < 0, \\ \frac{G^+_{i,j,k}+G^+_{i+1,j,k}}{|G_{i,j,k}|+|G_{i+1,j,k}|} & \text{otherwise,} \end{cases} \tag{26}$$

where $G^+ = \max(G_{i,j,k}, 0)$. Additional details can be found in [12] and [13].

Simulations of Charged Kerosene Jet

A charged liquid kerosene jet in quiescent air is simulated. A charge injection scheme is modeled, similar to that investigated by many researchers elsewhere [9, 7, 26, 3, 27, 28], and a schematic of the charge injection nozzle and multiphase flow domain is depicted in Fig. 1. Several different hydrodynamic inflows are qualitatively investigated: a bulk flow inlet, a fully turbulent inlet using a turbulent pipe preliminary simulation, and a realistic charge injection nozzle geometry used in experiments [6, 7, 8].

Bulk flow inlet

A charged liquid kerosene jet is simulated using a bulk inflow, with liquid injection through a circular port of diameter d_o. The properties for the simulation are inspired by charge injection experiments performed by Shrimpton and co-workers [7, 8, 29, 9]. Simulation parameters are summarized in Table 1, with the electro-inertial number defined as $\mathrm{N}_{ei} = q^2 d_o^2/\epsilon_r \epsilon_o \rho u^2$. The domain size is $L_x = 21d_o$, and $L_y = L_z = 7d_o$ discretized on a $768 \times 256 \times 256$ mesh. The boundary conditions implemented for this simulation are inflow and outflow conditions on the upstream and downstream $x-$faces, respectively, and zero electric potential on the $y-$ and $z-$faces. The interface is initialized as a liquid cylinder spanning the domain. Compared to experiments, the simulation employs a greater space charge in order to enhance liquid break-up in the absence of flow disturbances in the bulk inflow. In Figs. 2(a) and 2(b), a charge injection experiment performed by Shrimpton [10] and the charged simulation are shown side-by-side for comparison.

The multiphase simulation employing bulk inflow revealed that the domain size chosen for this simulation is too short in the lateral (y and z) directions. The domain size was increased from previous work used to study turbulent atomization of an uncharged Diesel jet to account for greater lateral dispersion resulting from the presence of space charge. However, Fig. 2(b) clearly shows that liquid struc-

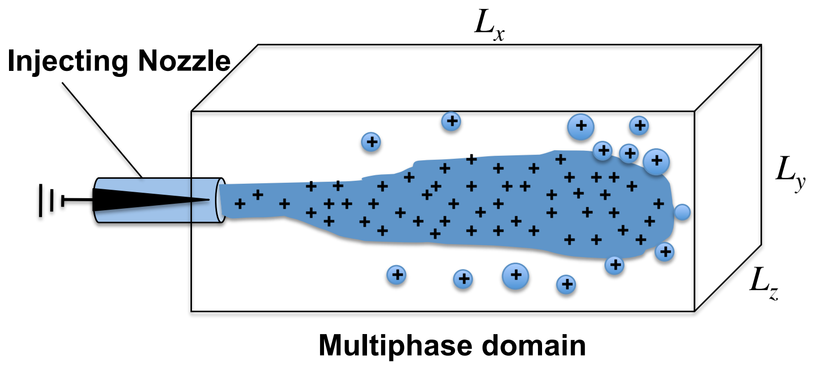

Figure 1. Sketch of computational domain employed in multiphase simulations.

Table 1. Parameters for charged liquid kerosene jet simulation employing bulk inflow. Total mesh size is 50.3 million grid points; d_o/h represents number of grid points across nozzle diameter.

Parameter	Simulation	Experiment
N_{ei}	1.25	0.1
Re	2000	4900
We	850	1700
d_o/h	25	n/a
ρ_l/ρ_g	652	
μ_l/μ_g	56	
ϵ_r	2.2	
γ [N/m]	0.0235	

tures reach the domain boundary near $x \approx 15d_o$. To remedy this issue, the domain size was increased for subsequent simulations.

While the bulk inflow simulation displays promising qualitative agreement with experiment, the quantity of electric charge employed in the simulation is much higher than experiment. Due to the high electric charge in a cylindrical jet and the boundary conditions on a rectangular domain, this simulation exhibits some evidence of mesh alignment. To explore this issue, a simple test is conducted to demonstrate the effect of the Coulomb force implementation. A two-dimensional simulation of a charged liquid cylinder in a rectangular domain is conducted. Simulations employ 2D periodic cylinders, $R_o = 0.1$, with Dirichlet boundary conditions for the electric potential ($\phi = 0$) on all four sides of a domain of $10R_o \times 10R_o$ with mesh spacing, R_o/h, set to 10. The relative permittivity is set to the value for kerosene, $\epsilon_r = \epsilon_l/\epsilon_g = 2.2$. The ratio of Coulomb force to surface tension takes the form of an electric Bond number, $N_E = q^2 r_o^3/\gamma\epsilon_o\epsilon_r$, and in this test N_E is set to 100, approximately one order of magnitude greater than experimental value in order to exaggerate the influence of the Coulomb force.

Two simulations are performed and evaluated. The first simulation employs a symmetric circular cylinder. Figure 3 displays the mesh alignment of the symmetric cylinder, with the Coulomb force stretching the interface non-uniformly toward the corners of the square domain. The other simulation employs a circular cylinder with a slightly disturbed surface. The surface disturbances are introduced using a cosine function for mode $m = 3$ and a disturbance amplitude equal to $R_o/500$. Also shown in Fig. 3 is the disturbed surface case, illustrating that the small disturbances are magnified by the Coulomb force. The surface is deformed in the direction of the three disturbances, commensurate with theory. Given the results of this test, we expect that the introduction of flow disturbances in the inflow, as well as lower levels of space charge, will eliminate any issues of mesh alignment.

Fully turbulent inlet

A second simulation is conducted with relevant non-dimensional parameters matched to Shrimpton's experiment, Case 2 [7]. Simulation parameters are summarized in Table 2. To introduce flow disturbances, a turbulent pipe preliminary simulation is performed and then used as the inflow to the multiphase simulation. The turbulent pipe preliminary simulation is performed with Re = 4900 to match the experimental value. To ensure fully developed turbulence, the inflow simulation is run until the axial skin friction coefficient, C_{f_x} reaches an approximately constant value, as depicted in Fig. 4. The

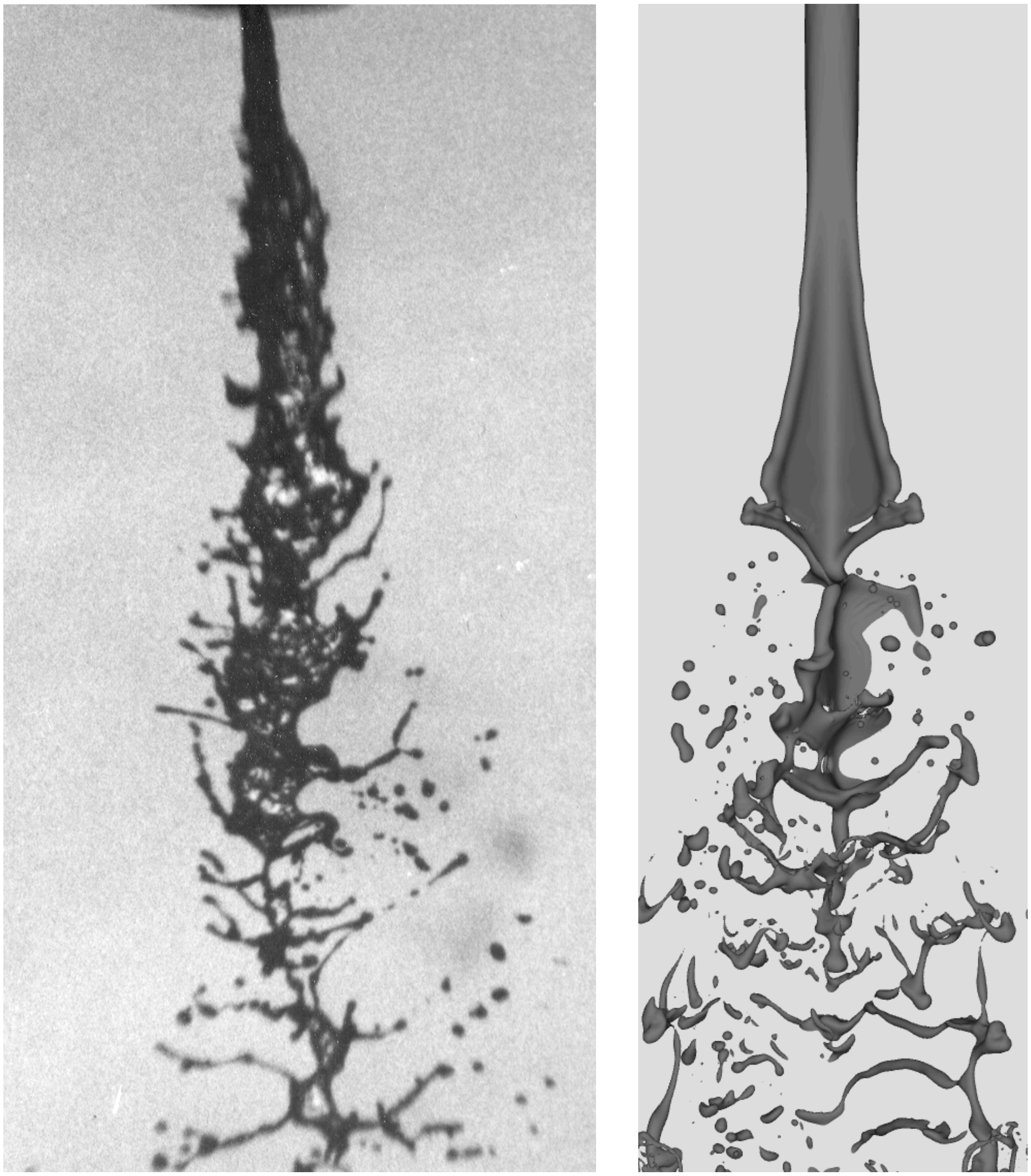

(a) Charge injection experiment, reproduced with permission [10].

(b) Charged simulation.

Figure 2. Charge injection experiment and simulation of charged liquid kerosene jet. Simulation initiated with bulk inflow. Experiment shadowgraph and simulation figure are not to scale.

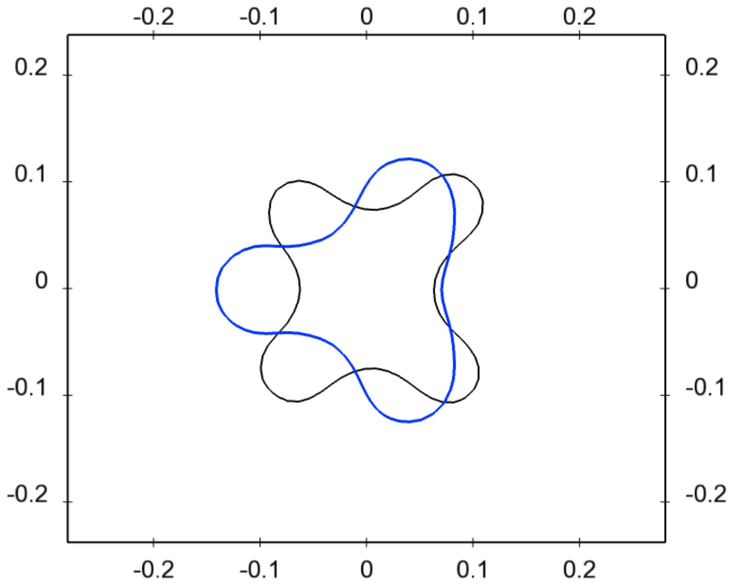

Figure 3. Evolution of initially perturbed interface (blue) and unperturbed interface (black) under the influence of the Coulomb force and surface tension.

simulation is run in cylindrical coordinates on a domain of $20d_0 \times d_o \times 2\pi$ and discretized on a mesh of $192 \times 96 \times 64$. As mentioned previously, the domain size was increased for this simulation from the $20d_o \times 7d_o \times 7d_o$ domain employed in the bulk inlet simulation to $20d_o \times 10d_o \times 10d_o$ in order to accommodate increased lateral dispersion.

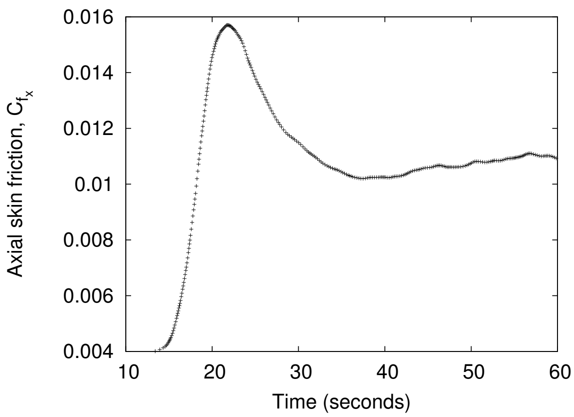

Figure 4. Axial skin friction coefficient for turbulent pipe preliminary inflow simulation.

Figures 5(a) and 5(b) compare Shrimpton's experiment [10] and the charged simulation. Unlike the bulk inflow case, the turbulent inflow shows no evidence of mesh alignment, attributable to lower levels of volumetric charge as well as the presence of flow disturbances introduced by the fully turbulent inflow that contribute to a non-uniform interface at the nozzle exit. The simulated jet shows more liquid disintegration than the experiment, especially near the axial centerline. The experiment shows the liquid core largely intact with satellite ligaments that begin to tear away from the core. The greater disintegration in the simulation may be due to the fully turbulent inflow, which appears to carry more turbulent kinetic energy and more flow disturbance than what is noticeable in the experiment shadowgraph, Fig. 5(a).

Table 2. Parameters for charged liquid kerosene jet simulation employing fully turbulent inflow.

Parameter	Simulation	Experiment
N_{ei}	0.1	
Re	4900	
We	1700	
d_o/h	25	n/a
ρ_l/ρ_g	652	
μ_l/μ_g	56	
ϵ_r	2.2	
γ [N/m]	0.0235	

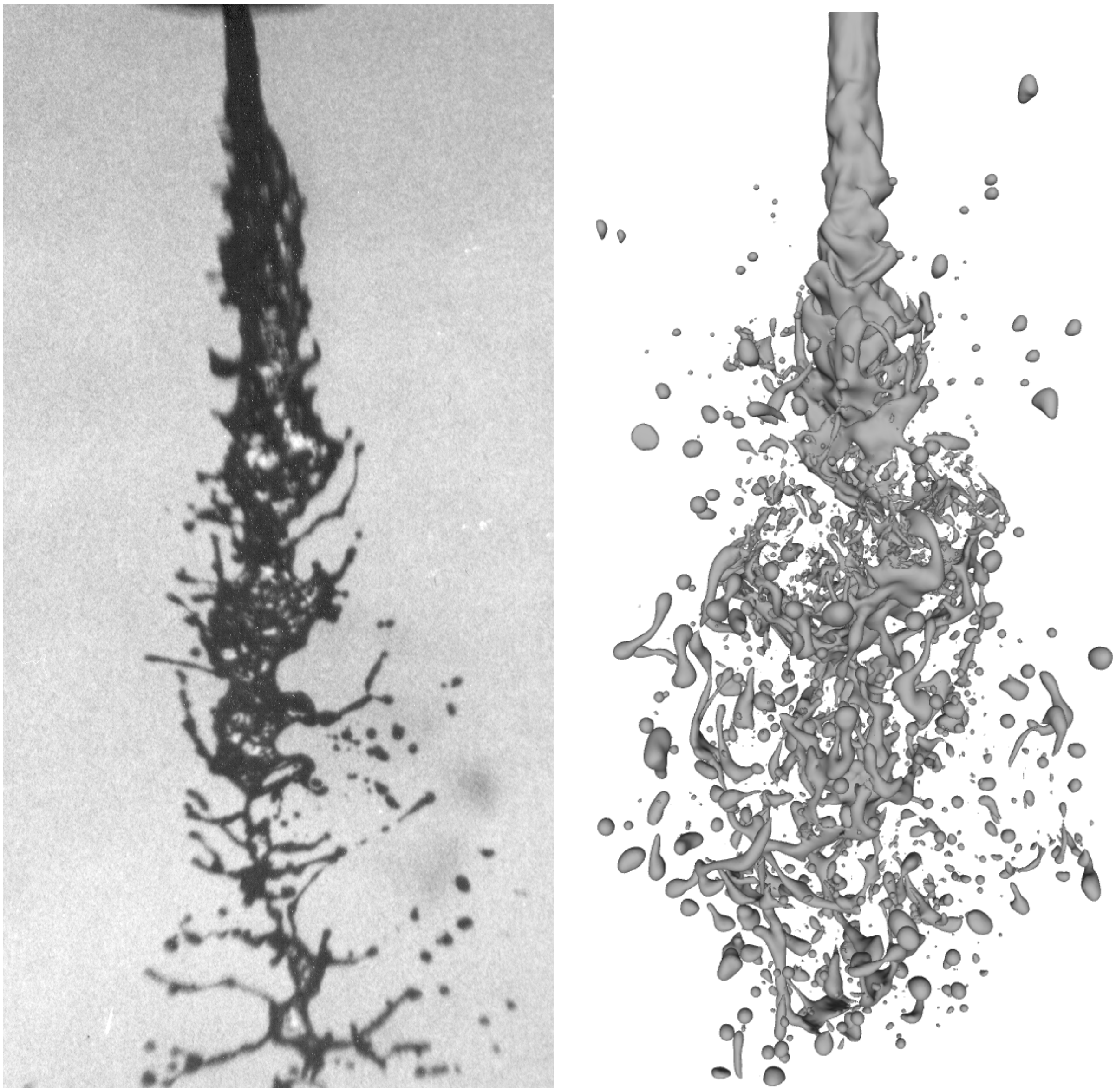

(a) Charge injection experiment, reproduced with permission [10].

(b) Charged multiphase simulation using fully turbulent inflow.

Figure 5. Comparison of experiment and simulation of charged liquid kerosene jet with turbulent inflow.

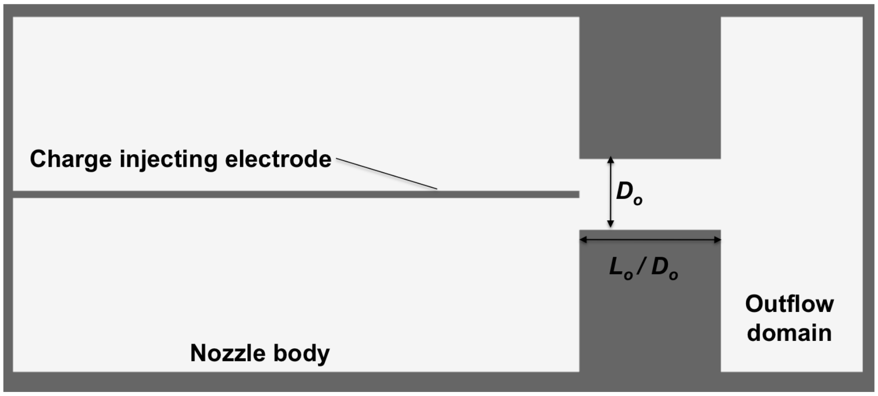

Figure 6. Charge injection nozzle geometry.

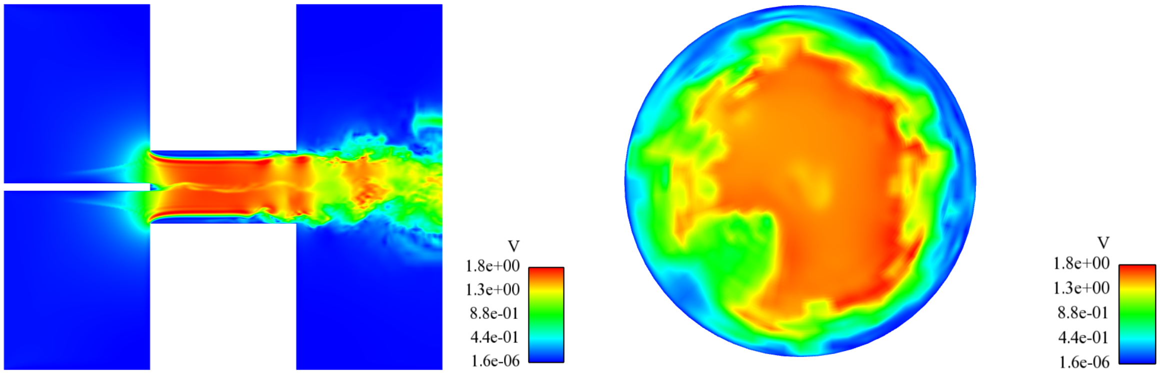

(a) Axial cut showing flow detail.

(b) Flow detail at the nozzle exit plane.

Figure 7. Charge injection nozzle preliminary inflow simulation results showing flow detail.

Charge injection nozzle inflow

A third inflow employs a preliminary simulation of a realistic charge injection nozzle. One of the nozzle geometries described in [6, 7, 8] is modeled. Figure 6 depicts the nozzle geometry. An outflow domain of reasonable extent is employed to fully capture three-dimensional effects at the nozzle exit plane. A simulation is performed in cylindrical coordinates with $\mathrm{Re} = 4900$ to match the experimental value. The domain shown in Fig. 6 is discretized on a $256 \times 128 \times 64$ mesh. Figure 7(a) illustrates the flow detail along an axial plane, and Fig. 7(b) shows flow detail at the nozzle exit plane, both clearly illustrating the three-dimensional nature of the flow at nozzle exit. As of paper publication, a multiphase simulation using this inflow had not yet been performed.

Conclusions

In this paper, a novel numerical scheme was used to simulate primary atomization for an electrically charged liquid hydrocarbon fuel. The computational scheme is implemented within a conservative finite difference scheme of high-order accuracy that employs state-of-the-art interface transport techniques ideally suited for simulating multiphase flows. The methodology was applied in direct numerical simulation of a charged liquid kerosene jet using a bulk inflow and qualitatively compared to experiements. To more accurately replicate hydrodynamic inflow conditions, preliminary simulations were conducted, including a fully turbulent pipe and a realistic charge injection nozzle used in experiment. Effects of bulk and fully turbulent inflow cases on the multiphase simulation were discussed.

Acknowledgments

The authors gratefully acknowledge the financial support from Army Research Office Contracts W911NF-08-C-0081 and W911NF-09-C-0157 under subcontract to TDA Research, Inc. Computational resources have been provided by NSF in the form of a Teragrid TRAC allocation for high-performance computing. The authors are thankful to Dr. John

S. Shrimpton, Energy Technology Research Group, University of Southampton, U.K., for many fruitful discussions about EHD and this work, and for his generous contribution of figures and experimental data.

References

[1] Environmental impacts of newly regulated non-road engines. Technical report, US Environmental Protection Agency, Feb 2002.

[2] B. Van Poppel, B. Spatafore, J.W. Daily, and J. Nabity. *47th Annual AIAA Aerospace Sciences Meeting*, 2009.

[3] K Kim and R Turnbull. *Journal of Applied Physics*, 47(5), May 1976.

[4] A Rigit and J Shrimpton. *Journal of Atomization and Sprays*, pp. 1–20, Dec 2006.

[5] A Rigit and J Shrimpton. *Journal of Atomization and Sprays*, 16:1–22, Dec 2006.

[6] J.S. Shrimpton and A.J. Yule. *Experiments in Fluids*, 26(5):460–469, Jan 1999.

[7] J.S. Shrimpton and A.J. Yule. *Journal of Atomization and Sprays*, 11:365–396, Feb 2001.

[8] J.S. Shrimpton and A.J. Yule. *Journal of Atomization and Sprays*, 13:173–190, Feb 2003.

[9] A.J Yule, J S Shrimpton, and W Watkins. *Fuel*, 74(7), Jul 1994.

[10] J.S. Shrimpton. *Int. J. Numer. Meth. Engng*, 58(3), Jan 2003.

[11] J.S. Shrimpton and Y. Laoonual. *Int. J. Numer. Meth. Engng*, 67(8), 2006.

[12] B. Van Poppel, O. Desjardins, and J.W. Daily. *submitted to Journal of Computational Physics*, 2010.

[13] B. Van Poppel, O. Desjardins, and J.W. Daily. *48th Annual AIAA Aerospace Sciences Meeting*. AIAA, January 5-8 2010.

[14] J. Chang, Arnold J. Kelly, and Joseph M. Crowley. *Handbook of electrostatic processes*. Marcel Dekker, Inc., Jan 1995.

[15] A. Kourmatzis and J. S. Shrimpton. *Journal of Atomization and Sprays*, 19:1045–1063, Dec 2009.

[16] O. Desjardins, G. Blanquart, G. Balarac, and H. Pitsch. *Journal of Computational Physics*, 227(15):7125–7159, 2008.

[17] Y. Morinishi, T.S. Lund, O.V. Vasilyev, and P. Moin. *Journal of Computational Physics*, 143(1):90–124, 1998.

[18] Y. Morinishi, O.V. Vasilyev, and T. Ogi. *Journal of Computational Physics*, 197(2):686–710, 2004.

[19] O.V. Vasilyev. *Journal of Computational Physics*, 157(2):746–761, 2000.

[20] Olivier Desjardins. PhD thesis, Jun 2008.

[21] J.E. Dendy. *Journal of Computational Physics*, 48:366–386, 1982.

[22] O. Desjardins, V. Moureau, and H. Pitsch. *Journal of Computational Physics*, 227, Jan 2008.

[23] O. Desjardins and H. Pitsch. *Journal of Computational Physics*, 228(5):1658–1677, Mar 2009.

[24] E. Olsson and G. Kreiss. *Journal of Computational Physics*, 210(1):225–246, 2005.

[25] R.P. Fedkiw, T. Aslam, B. Merriman, and S. Osher. *Journal of Computational Physics*, 152(2):457–492, 1999.

[26] A.J Kelly. *Journal of Aerosol Science*, 25(6), Mar 1994.

[27] W. Lehr and W. Hiller. *Journal of Electrostatics*, 30:433–440, May 1993.

[28] B. Spatafore, B. VanPoppel, J.W. Daily, and J. Nabity. *45th AIAA/ASME/ASEE Joint Propulsion Conference and Exhibit, Denver, Colorado*, Aug 2009.

[29] J.S. Shrimpton and A.J. Yule. *Journal of Atomization and Sprays*, 14:127–142, Feb 2004.